International Symposium
On Turbulence and Shear Flow
Phenomena (TSFP-9)
June 30 - July 3, 2015 *Melbourne, Australia*

OPTIMAL ENERGY GROWTH IN VARIABLE-DENSITY MIXING LAYERS AT HIGH ATWOOD NUMBER

Adriana Lopez-Zazueta, Jérôme Fontane* & Laurent Joly
Département Aérodynamique, Énergétique et Propulsion
Université de Toulouse - Institut Supérieur de l'Aéronautique et de l'Espace
10, Avenue édouard Belin, 31054 Toulouse, France
*Corresponding author: jerome.fontane@isae.fr

ABSTRACT

We analyze the influence of the specific features of variable-density Kelvin-Helmholtz (hereinafter quoted VDKH) roll-ups on the development of three-dimensional secondary instabilities. We use a direct-adjoint non-modal linear approach to determine the fastest growing perturbations over a single period of the time-evolving two-dimensional base-flow. Due to inertial (high Froude number) baroclinic sources of spanwise vorticity at high-Atwood number (up to $At = 0.5$ here), temporally evolving mixing-layers exhibit a layered structure associated with a strain field radically different from their homogeneous counterpart. It is found that additional mechanisms of energy growth are onset a little before the saturation time of the primary two-dimensional KH instability, corresponding to a substantial accumulated baroclinic spanwise vorticity in the base-flow. Beyond in time, the extra energy gain due to increasing Atwood numbers, relies both on the higher strain rate found in the vorticity enhanced braid and on contributions from spanwise baroclinic sources. Both effect are responsible for the organisation of the perturbation spanwise vorticity into elongated layers along the braid. They are associated to longitudinal velocity streaks that are responsible for the energy growth. This mechanism is boosting the energy gain over the whole range of spanwise wavenumbers but the short wavelength instabilities benefit more from the increase of the Atwood number than the long wavelength ones. Finally, it is observed that all optimal perturbations eventually triggers an hyperbolic-type instability, even at small spanwise wavenumber, where elliptic modes are favoured in the homogeneous case.

INTRODUCTION

Flows of interest to industrial applications or occurring spontaneously in nature are seldom homogeneous. Gas flows over obstacles at high velocities are subjected to variable temperature and density conditions due to the gas compressibility and viscous dissipation, but low-speed flows involved in heat-transfer or in species mixing are subjected to non-homogeneous inlet or boundary conditions resulting also in density variations in the bulk flow itself. The density contrast, namely the Atwood number $At \sim \Delta\rho/\rho_0$, may be very small but geophysical flows immersed in a gravity field are affected by buoyancy and their governing equations are liable to the Boussinesq approximation. For pairs of highly density-contrasted fluids, such as fuel-oxidizer candidates (*i.e.* methane-air, hydrogen-oxygen), the Atwood number rises up well beyond the Boussinesq approximation. In these flows, the vortex dynamics is affected by an inertial baroclinic vorticity production and departs largely from its homogeneous counterpart Joly *et al.* (2001).

As locally relevant to more complex flows, the mixing-layer paradigm, and its temporally evolving subset, is of central interest to these variable-density mixing flows. In this case, baroclinic vorticity production promotes a layered vorticity structure eventually replacing the KH roll-up with thin and wrapped vorticity sheets of alternate signs as the Atwood number is increased (Joly, 2002). The effect of this spanwise vorticity redistribution in the VDKH billows on its transition to three-dimensional motions was addressed by Fontane & Joly (2008) with a modal stability analysis. The linear response of the plane VDKH billow was demonstrated to be rich of a whole set of new secondary modes together with classical elliptical and hyperbolic modes with higher growth rates than those measured in the homogeneous KH billow. The two-dimensional secondary inflectional instability of the baroclinically-enhanced vorticity braid, elucidated by Reinaud *et al.* (2000), was nicely recovered in the linear analysis. However, this quasi-static approach based on a frozen approximation of the unsteady two-dimensional base flow is limited to perturbations growing faster than the time scale of the base flow unsteadiness. Given that these time scales are not clearly separated and that transient growth may benefit from the non-normality of the dynamical operator, there is a need to carry out a linear direct-adjoint non-modal analysis, well suited to determine the optimal energy growth of small perturbations over a temporally evolving VDKH billow. This is the aim of the present work. After a brief description of the base-flow and the numerical technique, we present the optimal perturbations and give a detailed analysis of the physical mechanisms responsible for their growth.

PROBLEM FORMULATION

The base-flow considered here consists of the Kelvin-Helmhotz instability which develops in a shear layer between two fluids of different densities with initial $tanh$ profiles (Fontane & Joly, 2008). We take u_0 half the velocity difference across the shear layer, $2l_0$ the shear layer depth and $\rho_0 = (\rho_{upper} + \rho_{lower})/2$ the mean density as characteristic velocity, length and density scales. The Reynolds number $Re = (u_0 l_0 \rho_0)/\mu$ is set to 1000 and the Atwood number

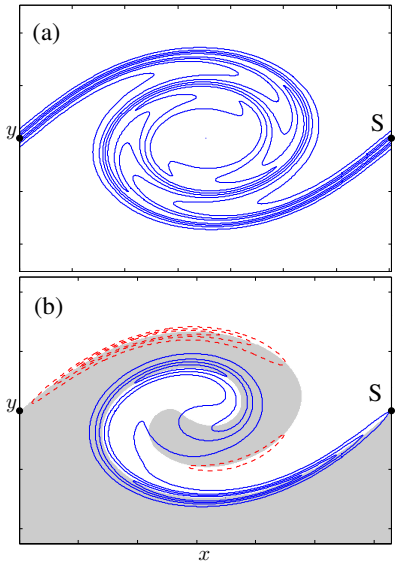

Figure 1. Base-flow spanwise vorticity field at the saturation time $t_{KH} = 30$ for (a) $At = 0$ and (b) $At = 0.5$. The gray-shaded region corresponds to the domain where the base-flow density is lower than ρ_0 and dashed contours correspond to positive values. Tick marks along x and y axis are separated by the initial vorticity thickness $2l_0$. The saddle point is denoted S. These conventions will hold throughout the paper.

$At = (\rho_{upper} - \rho_{lower})/2\rho_0$ varies in the range $At \in [0, 0.5]$. We address buoyancy-free flows where the Froude number, defined by $Fr = u_0/\sqrt{gl_0At}$ with g the gravity acceleration, is very large. The two-dimensional base-flow velocity $\boldsymbol{U} = (U_x, U_y)$ and density R fields of the VDKH billows are obtained through non-linear direct numerical simulations of the shear layer perturbed with the most amplified Kelvin-Helmholtz linear mode. The amplitude of the primary KH instability is set such that non-linear saturation occurs at $t_{KH} = 30$, see Lopez-Zazueta *et al.* (2015) for details about the numerical procedure. The density variations induce strong modifications in the development of the KH primary wave due to the baroclinic vorticity production (Joly *et al.*, 2001). The main feature lies in the asymmetric reorganisation of the the base-flow vorticity field into two sheets of opposite sign holding high level of strain and located on either side of the braid saddle point, as displayed in figure 1.

We look for three-dimensional linear perturbations of the form $[u_x, u_y, iu_z, p, \rho](x,y,t)e^{ikz}$, with k the spanwise wavenumber, that are likely to grow on top of the VDKH billows. We solve iteratively the linearised direct-adjoint Navier-Stokes equations for the velocity and density perturbations fields, see Lopez-Zazueta *et al.* (2015) for a detailed presentation of the equations, methodology and numerics. The optimisation loop is aimed for the maximisation over all possible initial conditions with zero density perturbation of the perturbation kinetic energy gain $\mathscr{G}_E(T, t_0) = \max(E(T)/E(t_0))$ over the period $[t_0, T]$ where t_0 and T are respectively called injection and horizon times. In the following, we only present the case where $t_0 = 0$ and $T = 40$. The influence of the frame of optimisation is considered in Lopez-Zazueta *et al.* (2015). The kinetic energy

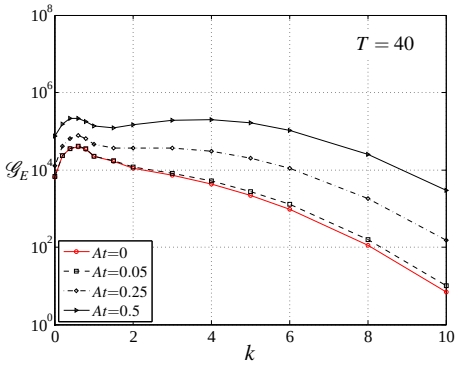

Figure 2. Optimal energy gain $\mathscr{G}_E$ at $T = 40$ as a function of the spanwise wavenumber k for four values of the Atwood number.

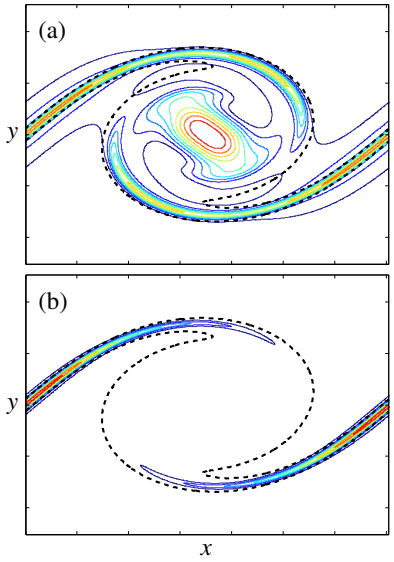

Figure 3. Energy field of the homogeneous optimal perturbation at t_{KH} with (a) $k = 0.6$ and (b) $k = 4$. The dashed contour corresponds to 20% of the maximal absolute value of the base-flow vorticity $|\Omega_m|$

of the perturbation is classically defined by

$$E = \frac{1}{2}\iint (u_x u_x^* + u_y u_y^* + u_z u_z^*)\, dxdy$$

where the integration is performed on the computational domain and $*$ stands for the complex conjugate.

OPTIMAL PERTURBATIONS

Figure 2 shows the optimal energy gain $\mathscr{G}_E$ at $T = 40$ versus spanwise wavenumber for $At = 0, 0.05, 0.25$ and 0.5. One can see that density effects result in a significant increase of $\mathscr{G}_E$ for all k. In the homogeneous case, long wavelength perturbations present energy gains significantly higher than large wavenumber ones. As already observed by Arratia *et al.* (2013), we find that the former trigger elliptic modes which develop mainly within the core

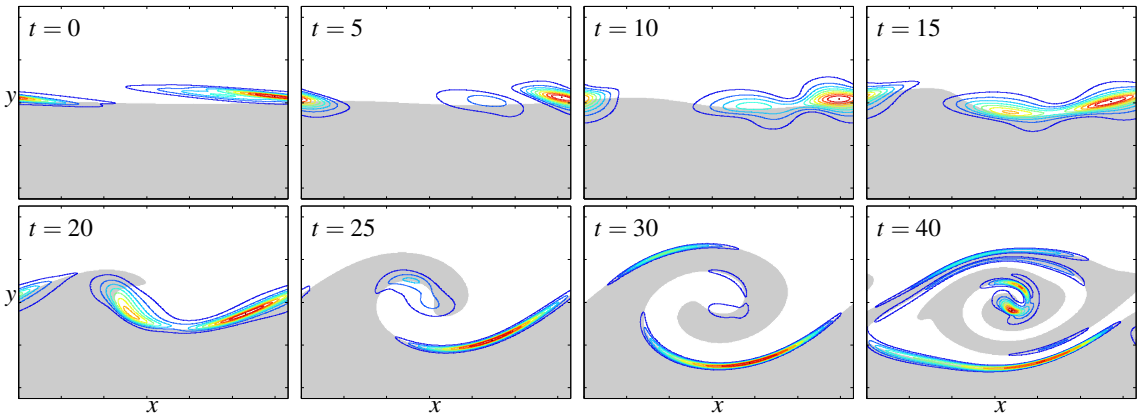

Figure 4. Temporal evolution during $[0,T]$ of the energy field for the global optimal perturbation with $k = 0.6$ and $At = 0.5$.

of the KH billow while the latter give rise to the hyperbolic modes which are located along the braid, see figure 3. When the Atwood number increases up to $At = 0.5$, small wavenumber perturbations remain the most amplified but large wavenumber hyperbolic ones benefit more from the increase of the Atwood number, with a gain increasing by more than two orders of magnitude for the largest wavenumbers explored. For all Atwood numbers, the overall maximum energy gain, usually quoted as the global optimal perturbation, is always found for $k = 0.6$.

Global optimal perturbation

We now focus on this global optimal perturbation for the most density-contrasted case in order to decipher the physical mechanisms at play in the observed enhancement of the energy growth. Figure 4 displays the evolution of its kinetic energy field. The initial perturbation consists in a thin layer centred around the hyperbolic saddle point and aligned with the direction of maximum compression of the base-flow. The layer is progressively deformed under the base-flow mean shear so that it is realigned in the direction of maximum stretching by $t_b \approx 20$. This kinematic evolution is typical of the so-called Orr mechanism of transient energy growth. Then the perturbation concentrates into two thin layers along the braid where lies the base-flow baroclinic vorticity production. This pattern is characteristic of hyperbolic instability which takes over the elliptic mode found in the homogeneous case for such a small wavenumber. The change of nature for the perturbation concords with the modal analysis of Fontane & Joly (2008) which showed that the elliptic mode was not detected amongst the most amplified modes for $At = 0.5$.

Figure 5 displays the temporal evolution of the global optimal energy gain for the four values of the Atwood number considered here. For non-zero Atwood numbers, the extra energy gain onsets around a bifurcation time $t_b \approx 20$, a little before the saturation of the VDKH billow at $t_{KH} = 30$, leaving perturbations insensitive to density effects during the early development of the base-flow. The evolution of the perturbation is thus clearly divided into two stages: an initial one $[t_0,t_b]$ with a unique route for optimal energy growth whatever the Atwood number, and a second one $[t_b,T]$ where density variations have an influence on the development of the perturbation. Looking at the evolution of the primary KH mode, the first stage corresponds the linear quasi-parallel evolution of the base-flow, whereas the VDKH wave enter the non-linear regime and rolls up in the second stage (Lopez-Zazueta, 2015).

In order to identify the physical mechanisms responsible for the perturbation growth, we look more precisely at the evolution equation for the growth rate of the perturbation $\sigma_E = \frac{1}{E}\frac{dE}{dt}$ which is obtained straightforwardly from the transport equation for the kinetic energy:

$$\frac{dE}{dt} = \Pi_1 + \Pi_2 + \Pi_3 + \Pi_4 + \Pi_\phi$$

where $\Pi_1, \Pi_2, \Pi_3, \Pi_4$ and Π_ϕ are respectively the extraction of energy from the base-flow shear, the extraction of energy from the base-flow strain field, the production/destruction of energy through dilatation/compression, the production/destruction of energy through variable-density effects and the viscous dissipation. They read (Lopez-Zazueta, 2015):

$$\begin{aligned}
\Pi_1 &= -\iint u_x u_y \left(\frac{\partial U_x}{\partial y} + \frac{\partial U_y}{\partial x}\right) dxdy \\
\Pi_2 &= \frac{1}{2}\iint \left(u_x^2 - u_y^2\right)\left(\frac{\partial U_x}{\partial x} - \frac{\partial U_y}{\partial y}\right) dxdy \\
\Pi_3 &= \iint \frac{1}{R}\left(u_x\frac{\partial p}{\partial x} + u_y\frac{\partial p}{\partial y} + u_z\frac{\partial p}{\partial z}\right) dxdy \\
&\quad - \iint \frac{\rho}{R^2}\left(u_x\frac{\partial P}{\partial x} + u_y\frac{\partial P}{\partial y} + u_z\frac{\partial P}{\partial z}\right) dxdy \\
\Pi_4 &= \frac{1}{2}\iint u_z^2\left(\frac{\partial U_x}{\partial x} + \frac{\partial U_y}{\partial y}\right) dxdy \\
\Pi_\phi &= \frac{1}{Re}\iint \Phi_E \, dxdy .
\end{aligned}$$

Among them, Π_3 and Π_4 are specific to the inhomogeneous situation. Because Π_4 term has been found to be very small, it is combined to Π_2 in the results presented in the following.

Figure 6 shows the temporal evolution of all these contributions for $At = 0$ and $At = 0.5$. Before t_b, the kinetic energy budget follows the same evolution in both cases. The homogeneous evolution is in excellent agreement with the one obtained by Arratia *et al.* (2013), see their figure 7. During the initial period $[t_0,t_b]$, the perturbation growth is due to the energy extraction from the base-flow shear. As observed by Arratia *et al.* (2013), the Orr mechanism

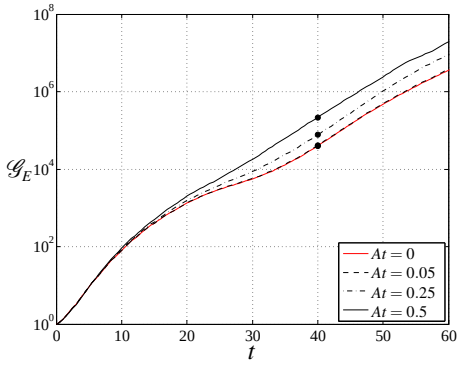

Figure 5. Temporal evolution of the energy gain $\mathscr{G}_E$ of the global optimal perturbation at various Atwood numbers. The bullet points denote the horizon time.

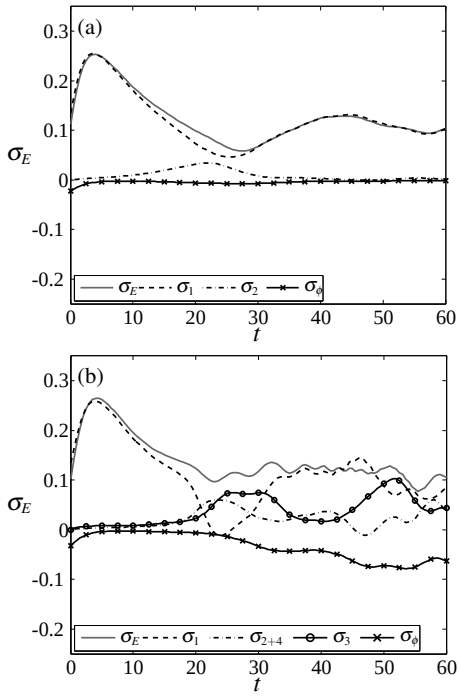

Figure 6. Temporal evolution of the kinetic energy growth rate σ_E and its different contributions during $[t_0, 60]$ for the global optimal perturbation at (a) $At = 0$ and (b) $At = 0.5$.

of transient energy growth is responsible for the initial development of the perturbation with $k = 0.6$, which corresponds to the early evolution of the layer depicted above in figure 4. Shortly after t_b, the evolution departs significantly from its homogeneous counterparts where energy growth is essentially due to base-flow shear conversion. In the inhomogeneous flow, the production/destruction term Π_3 specific to the variable-density situation becomes active and modify notably the energy growth of the perturbation along with the energy conversion from the base-flow strain Π_2 which takes over the shear extraction term Π_1. Compared to the homogeneous case, the increase of the Atwood number results also in an increase of the viscous dissipation which is largely compensated by Π_2 and Π_3 terms since an extra gain of energy is observed. The identification of the two terms Π_2 and Π_3 as being the source of energy growth

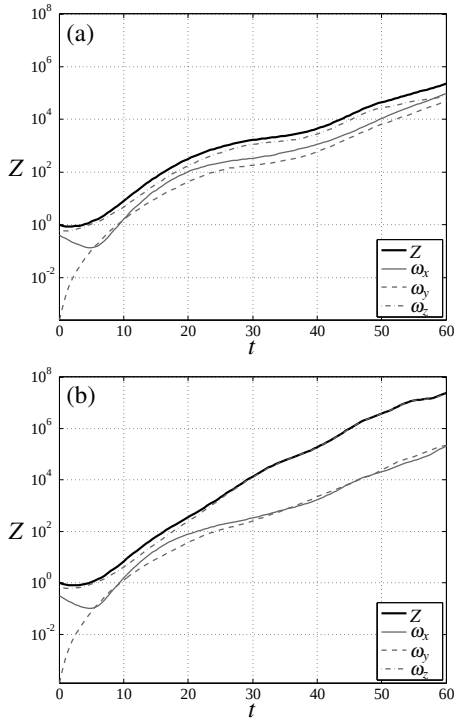

Figure 7. Temporal evolution of the enstrophy Z and the relative contribution of each vorticity component ω_x, ω_y and ω_z for the global optimal perturbation at (a) $At = 0$ and (b) $At = 0.5$.

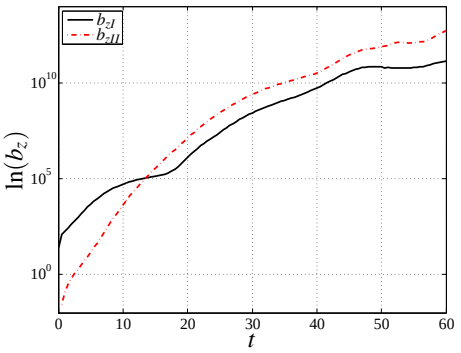

Figure 8. Temporal evolution of the two components of the spanwise linearised baroclinic torque b_z for the global optimal perturbation at $At = 0.5$.

does not explain the physical mechanism behind them. This is the object of the next section.

The physical mechanism of extra energy growth

The Π_3 term responsible for the extra energy gain is the trace in the kinetic energy equation of the baroclinic torque $\boldsymbol{b}$ which becomes active in the vorticity transport equation as soon as density variations are present. If we look at the evolution of the perturbation enstrophy and its repartition between the vorticity components in figure 7, it can be observed in the inhomogeneous case that the growth of enstrophy after t_b is only due to the increase of the spanwise

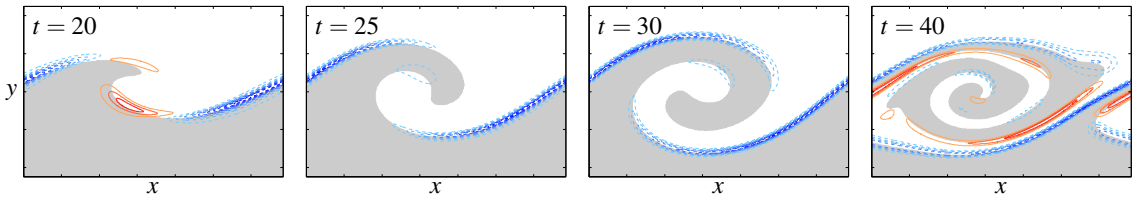

Figure 9. Temporal evolution during time interval $[t_b, T]$ of the density field for the global optimal perturbation at $At = 0.5$. Dashed contours correspond to negative values.

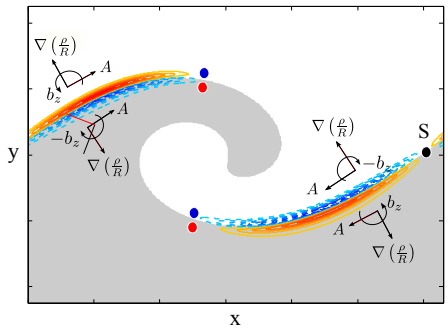

Figure 10. Spanwise component of the linear baroclinic torque b_z at $t = 25$ with a schematic representation of the term b_{zII} sketched on top of it. Red and blue dots indicate the local sign of the spanwise vorticity of the perturbation before the action of the baroclinic torque.

vorticity component ω_z. Compared to the homogeneous situation, not only there is an extra gain of enstrophy but the anisotropy in favour of ω_z is also strengthened. This increase of ω_z is linked with the spanwise component b_z of the linearised baroclinic torque which writes as the sum of the two following terms (Lopez-Zazueta *et al.*, 2015):

$$b_z = \underbrace{a_x \frac{1}{R}\frac{\partial R}{\partial y} - a_y \frac{1}{R}\frac{\partial R}{\partial x}}_{b_{zI}} \underbrace{A_x \frac{\partial}{\partial y}\left(\frac{\rho}{R}\right) - A_y \frac{\partial}{\partial x}\left(\frac{\rho}{R}\right)}_{b_{zII}}.$$

where $\boldsymbol{A}$ and $\boldsymbol{a}$ are the acceleration fields of the base-flow and the perturbation respectively. Figure 8 displays the temporal evolution of these two terms. After t_b, the second term b_{zII} is responsible for the essential of the spanwise baroclinic vorticity production. It corresponds to the cross product between the two-dimensional base-flow acceleration field and the perturbation density field. Looking at the evolution of the perturbation density field during $[t_b, T]$ in figure 9, one can see that it is mainly structured in a thin layer located along the braid. Combined with the two-dimensional hyperbolic base-flow acceleration field in the braid region, it results in a spanwise baroclinic torque organised into a antisymmetric quadrupole centred on the braid saddle point as plotted in figure 10 at $t = 25$, along with a sketch of the contributions of b_{zII}. Before t_b, the spanwise perturbation vorticity field ω_z is structured into two layers of opposite sign located along the braid, as it can be seen at $t = 15$ in figure 11. Thus, in the part of the braid located on the left side of the saddle point, the two baroclinic sink and source are of the same sign as the perturbation spanwise vorticity ω_z denoted by the bullet points in figure 10. This results in an enhancement of the two existing layers. Conversely, in the part of the braid located on the right side of the saddle point, the two baroclinic sink and source are of opposite sign to the one of ω_z. This results in a destructive contribution of b_z to the two layers. As illustrated in figure 11, the action of the spanwise baroclinic torque on the right part of the braid results first in the destruction of the initial two layers followed by the appearance of two layers of opposite sign which are readily observable at $t = 25$. By $t = 30$, the spanwise vorticity field of the perturbation is structured on each side of the saddle point into two elongated thin layers. This pattern is characteristic of a longitudinal jet which is confirmed by looking at the perturbation longitudinal velocity field u_x in figure 11. At $t = 30$, it consists of two streaks of opposite sign located along the braid on either side of the saddle point. These streaks are responsible for the essential of the perturbation energy growth as shown in figure 12. While the contribution of each velocity component to the energy growth is isotropic in the homogeneous case, the energy growth is essentially due to the increase of the longitudinal velocity component in the variable-density case. This is corroborated by a similar evolution of the structure for both the longitudinal velocity field and the energy field in figure 4 and 11.

The above physical mechanism for energy growth of the global optimal perturbation relying on spanwise baroclinic vorticity production is generic for all the optimal perturbations identified here whatever the value of the spanwise wavenumber. A similar analysis is performed for the large wavenumber perturbation in Lopez-Zazueta (2015).

CONCLUSIONS

We performed a non-modal stability analysis of the variable-density Kelvin-Helmholtz billow looking for the optimal perturbations maximising the growth of kinetic energy. It is observed that the optimal energy gain is insensitive to the Atwood number during an initial stage $[t_0, t_b]$ corresponding to the quasi-parallel linear phase of the primary wave. There the global optimal perturbation benefits from base-flow shear conversion through the so-called Orr mechanism. After the bifurcation time t_b, the optimal gain is increased with the Atwood number. Contrary to the homogeneous case (Arratia *et al.*, 2013), the optimal perturbation triggers the hyperbolic instability whatever the value of the spanwise wavenumber. The extra energy gain is associated with the appearance of longitudinal velocity streaks along the baroclinically-enhanced vorticity braid. These streaks result from the baroclinic production of two thin layers of spanwise vorticity along the braid, specifically due to the combination of the base-flow acceleration field and the perturbation density field. It is remarkable to note that variable-density effects in the base-flow do not promote the strength of streamwise vortices, so far accepted as the

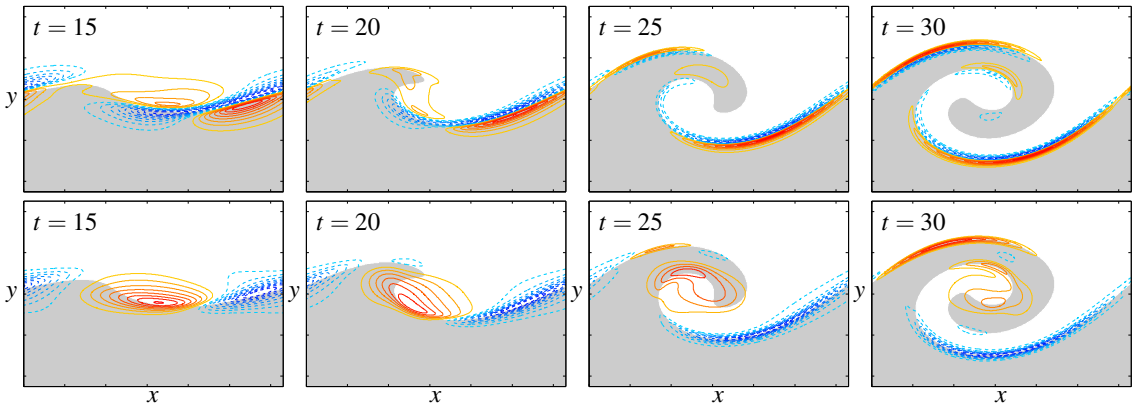

Figure 11. Temporal evolution during time interval $[15,30]$ of the spanwise vorticity component ω_z (upper) and the longitudinal velocity component u_x (lower) for the global optimal perturbation at $At = 0.5$.

paradigm for three-dimensionalisation of free shear flows.

The maximisation of the kinetic energy gain chosen here is not the only available criterion to figure out the influence of density effect on the development of such perturbations. Maximisation of enstrophy or mixing (Foures *et al.*, 2014) would impose different conditions on the baroclinic vorticity production and density field that might be worth to scrutinise in a future extension of this work.

REFERENCES

Arratia, C., Caulfield, C. P. & Chomaz, J.-M. 2013 Transient perturbation growth in time-dependent mixing layers. *J. Fluid Mech.* **717**, 90–133.

Fontane, J. & Joly, L. 2008 The stability of the variable-density Kelvin–Helmholtz billow. *J. Fluid Mech.* **612**, 237–260.

Foures, D. P. G., Caulfield, C. P. & Schmid, P.J. 2014 Optimal mixing in two-dimensional plane poiseuille flow at infinite péclet number. *J. Fluid Mech.* **748**, 241–277.

Joly, L. 2002 The structure of some variable density shear flows. In *Variable density Fluid turbulence*. Kluwer.

Joly, L., Reinaud, J.N. & Chassaing, P. 2001 The baroclinic forcing of the shear layer three-dimensional instability. *2nd Int. Symp. on Turbulence and Shear Flow Phenomena, Stockholm* **3**, 59–64.

Lopez-Zazueta, A. 2015 Stabilité secondaire non-modale d'une couche de mélange inhomogène. PhD thesis, Université de Toulouse, Institut Supérieur de l'Aéronautique et de l'Espace.

Lopez-Zazueta, A., Fontane, J. & Joly, L. 2015 Optimal perturbations in time-dependent variable-density Kelvin–Helmholtz billows. *submitted to J. Fluid Mech.* .

Reinaud, J., Joly, L. & Chassaing, P. 2000 The baroclinic secondary instability of the two-dimensional shear layer. *Phys. Fluids* **12** (10), 2489–2505.

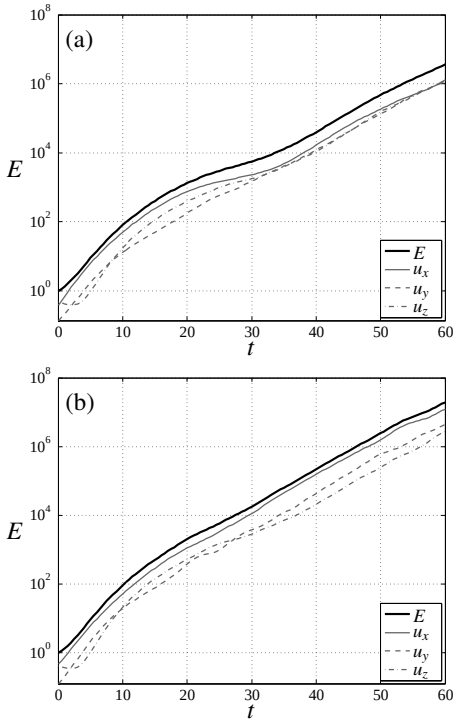

Figure 12. Temporal evolution of the kinetic energy E and the relative contribution of each velocity component u_x, u_y and u_z for the global optimal perturbation at (a) $At = 0$ and (b) $At = 0.5$.